Journal Name

ARTICLE TYPE

Cite this: DOI: 10.1039/xxxxxxxxxx

Electron paramagnetic resonance study of ferroelectric phase transition and dynamic effects in Mn^{2+} doped $[NH_4][Zn(HCOO)_3]$ hybrid formate framework

Marius Navickas,[a] Laisvydas Giriūnas,[a] Vidmantas Kalendra,[a] Timur Biktagirov,[b] Uwe Gerstmann,[b] Wolf Gero Schmidt,[b] Mirosław Mączka,[c] Andreas Pöppl,[d] Jūras Banys,[a] Mantas Šimėnas*[a]

Received Date
Accepted Date

DOI: 10.1039/xxxxxxxxxx

www.rsc.org/journalname

We present X- and Q-band continuous wave (CW) and pulse electron paramagnetic resonance (EPR) study of manganese doped $[NH_4][Zn(HCOO)_3]$ hybrid framework, which exhibits a ferroelectric structural phase transition at 190 K. The CW EPR spectra obtained at different temperature exhibit clear changes at the phase transition temperature. This suggests a successful substitution of the Zn^{2+} ions by the paramagnetic Mn^{2+} centers, which is further confirmed by the pulse EPR and ^1H ENDOR experiments. Spectral simulations of the CW EPR spectra are used to obtain the temperature dependence of the Mn^{2+} zero-field splitting, which indicates a gradual deformation of the MnO_6 octahedra indicating a continuous character of the transition. The determined data allows us to extract the critical exponent of the order parameter ($\beta = 0.12$), which suggests a quasi two-dimensional ordering in $[NH_4][Zn(HCOO)_3]$. The experimental EPR results are supported by the density functional theory calculations of the zero-field splitting parameters. Relaxation time measurements of the Mn^{2+} centers indicate that the longitudinal relaxation is mainly driven by the optical phonons, which correspond to the vibrations of the metal-oxygen octahedra. The temperature behavior of the transverse relaxation indicates a dynamic process in the ordered ferroelectric phase.

1 Introduction

Metal-organic frameworks (MOFs) are extensively studied hybrid materials due to their potential application in gas storage and separation devices[1], drug delivery systems[2] and multiferroic memory devices[3–5]. These coordination networks are formed from various organic linker molecules and metal centers that constitute porous structures. In the so-called dense MOFs, the pore system inherently confines molecules, which are tightly bound to the framework[6].

The most popular class of dense MOFs is $[A][M(HCOO)_3]$ metal-formates, which often exhibit interesting ferromagnetic and ferroelectric-like properties[3–5,7–16]. The metal centers M^{2+} (usually transition metal, Zn^{2+}, Cd^{2+} and Mg^{2+} ions) in these compounds are connected via the formate linkers into anionic frameworks containing MO_6 octahedra[9–11,13,14]. Such porous structures confine molecular cations A^+ such as $(CH_3)_2NH_2^+$[3–5,7,9,10] or NH_4^+[11–13]. The common property of the majority of formate frameworks are structural order-disorder phase transitions related to the cooperative molecular cation ordering[7,9–11,13,14].

The most studied formate frameworks contain dimethylammonium ($(CH_3)_2NH_2^+$) cations and have a perovskite structure[3,5,7,9,10,17–21]. Despite many studies, a proper ferroelectric response in these compounds is highly questionable[22]. In contrast, a clear ferroelectric behavior has been reported in $[NH_4][M(HCOO)_3]$ frameworks containing ammonium (NH_4^+) cations[11,15,23]. These compounds usually crystallize in a much less common $4^9 \cdot 6^6$ chiral structural topology[24] with one exception of $[NH_4][Cd(HCOO)_3]$ framework having a $4^{12} \cdot 6^3$ topology and a perovskite structure[25].

An important example of these frameworks is $[NH_4][Zn(HCOO)_3]$ (AmZn), which undergoes a structural phase transition at about $T_0 = 190$ K accompanied by the ammonium cation ordering and change in the space group from $P6_322$ in the high temperature (HT) phase ($T > T_0$) to the polar $P6_3$ in the low temperature (LT) phase ($T < T_0$)[23]. The crystal structure of AmZn at 290 K (HT phase) and 110 K (LT phase) is presented

[a] Faculty of Physics, Vilnius University, Sauletekio av. 9, LT-10222 Vilnius, Lithuania; E-mail: mantas.simenas@ff.vu.lt
[b] Department of Physics, Paderborn University, Warburger 100, D-33098 Paderborn, Germany
[c] Institute of Low Temperature and Structure Research, Polish Academy of Sciences, P.O. Box-1410, PL-50-950 Wroclaw 2, Poland
[d] Felix Bloch Institute for Solid State Physics, Leipzig University, Linnestrasse 5, D-04103 Leipzig, Germany

in Figure 1. The structure shows a three-dimensional chiral anionic $Zn(HCOO)_3^-$ framework having the aforementioned $4^9 \cdot 6^6$ topology with arrays of NH_4^+ cations located within the helical channels along the c axis[23]. In the HT phase, the NH_4^+ cation is trigonally disordered (Figure 1a), while it is ordered in the LT phase (Figure 1b)[23].

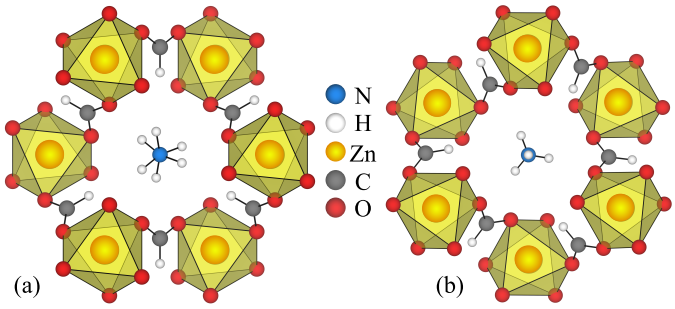

Fig. 1 The crystal structure of AmZn framework at (a) 290 K (HT phase) and (b) 110 K (LT phase) along the $\bar{c}$ axis. Structural data is taken from Ref. [23].

The dielectric spectroscopy and differential scanning calorimetry measurements[11,23], Raman and IR spectroscopy[13,26], Brillouin scattering[12] and NMR studies[27] of AmZn relate the mechanism of the phase transition to the NH_4^+ cation ordering. Moreover, the phase transition seems to have a continuous second-order character[11,13]. The electric polarization measurements indicate that the phase transition occurs from the paraelectric to the ferroelectric phase[23]. Despite these studies, there are still many unanswered questions about the mechanism and universality class of the continuous phase transition in these compounds. Therefore, there is a need for other experimental methods that can locally probe the structural phase transition.

One of such methods is electron paramagnetic resonance (EPR) spectroscopy, which has proved to be highly effective for studying the structural phases and phase transitions in perovskite formate frameworks[17–19,28,29]. In order to investigate the diamagnetic frameworks with EPR, a doping with paramagnetic probe ions is required. The concentration of these ions is usually maintained very low to avoid altering of the material properties. The paramagnetic Mn^{2+} centers have proven to be especially suitable for such studies, as they easily replace Zn^{2+} ions in the frameworks, have rather long electron spin coherence time and substantial zero-field splitting, which is highly sensitive to the local structural changes[18,19,28].

In this work, we present a combined continuous wave (CW), pulse EPR and pulse electron nuclear double resonance (ENDOR) study of AmZn framework doped with a small amount of paramagnetic Mn^{2+} ions. The CW EPR experiments allow us to study and characterize the ferroelectric phase transition. The obtained results are supported by the density functional theory (DFT) calculations of the zero-field splitting. The CW EPR experiments probe only the first coordination shell of the paramagnetic center prohibiting detection of much weaker hyperfine interactions of the distant nuclei. In order to study these interactions, we use pulse EPR and ENDOR techniques[30,31]. The measurements of the longitudinal relaxation and phase memory time of Mn^{2+} are also performed to investigate the lattice and molecular dynamics in the ferroelectric phase of AmZn.

2 Experimental and Computational Methods

2.1 Sample Preparation

$ZnCl_2$ (98%, Fluka), $[NH_4][HCOO]$ (99%, Fluka), formic acid (98%, Fluka), and methanol (99.8%, Aldrich) were commercially available and used without further purification. AmZn: 0.1 Mn^{2+} mol% was obtained by a slow diffusion method. In a typical experiment, 20 mL methanol solution containing 20 mmol of $[NH_4][HCOO]$ and 20 mmol of formic acid was placed at the bottom of a glass tube (20 mm inner diameter). 30 mL of methanol solution containing 1.998 mmol of $ZnCl_2$ and 0.002 mmol of $MnCl_2$ was gently added to the solution. The tube was sealed and kept undisturbed. The colorless crystals were harvested after 1 week, washed three times with methanol, and dried at room temperature.

2.2 EPR and ENDOR Spectroscopy

The X- (∼9.5 GHz) and Q-band (∼35 GHz) CW EPR experiments were performed using Bruker E580 and Bruker EMX 10-40 spectrometers, respectively. The amplitude and frequency of the modulating field were set to 4 G and 100 kHz. The microwave power was adjusted at each temperature to avoid signal saturation.

X-band pulse EPR experiments were performed using Bruker E580 EPR spectrometer equipped with Bruker MD-5 resonator. For pulse EPR measurements at Q-band frequency, Bruker SuperQFT-u Q-band extension of the E580 microwave bridge was used together with Bruker EN5107D2 microwave resonator. The two-pulse (2p) echo-detected field sweep experiments were performed using a Hahn echo pulse sequence ($\pi/2-\tau-\pi-\tau-$echo). For the three-pulse (3p) electron spin echo envelope modulation (ESEEM) measurements[32], the $\pi/2-\tau-\pi/2-\tau'-\pi/2-\tau-$echo pulse sequence was used. The baselines of the obtained ESEEM time domain patterns were corrected by subtracting exponential decays. The remaining time domain signals were zero-filled and Fourier transformed to obtain the frequency domain ESEEM spectra. The longitudinal relaxation time T_1 was determined using the inversion recovery pulse sequence ($\pi-\tau'-\pi/2-\tau-\pi-\tau-$echo)[30]. The phase memory time T_m was obtained using a Hahn echo pulse sequence.

The pulse ENDOR experiments were performed using Bruker DICE ENDOR system equipped with Bruker EN4118X-MD4 and WEN5107D2 resonators. The Davies ENDOR pulse sequence[33] was used with the radio frequency pulses of 8 and 13 μs at X- and Q-band frequency, respectively. All pulse experiments were performed by using 16 ns $\pi/2$ microwave pulses.

All EPR experiments were performed on vacuum-sealed powder samples. The temperature was measured using a T-type thermocouple pressed near the sample outside an EPR tube. Simulations of the EPR and ENDOR spectra were performed using EasySpin 5.2.25 software[34].

2.3 DFT Calculations

We used QUANTUM ESPRESSO DFT package[35,36] to calculate the zero-field splitting parameters of the Mn^{2+} centers in AmZn. Exchange-correlation effects of the electronic system were described with the semilocal PBEsol functional[37] complemented with the D2 dispersion correction[38]. The plane-wave basis set with an energy cutoff of 80 Ry and the norm-conserving pseudopotentials were adopted to treat the valence electrons. In particular, 3s, 3p, and 3d states of the Mn atom were included in the valence. In the LT phase of AmZn, a 216-atom supercell ($1\times1\times2$) of the host material was adopted with one Zn atom being substituted with Mn. The structural relaxation was carried out with the fixed lattice constants determined experimentally in Ref.[23] at 110 K.

To obtain accurate estimates of the spin Hamiltonian parameters, we used the projector augmented wave (PAW) method as implemented in the GIPAW module of QUANTUM ESPRESSO[36]. We took into account correlation effects of the strongly localized Mn 3d electrons by employing the Hubbard correction (DFT+U approach) with the self-consistently determined $U = 4.59$ eV[39]. The zero-field splitting tensor was evaluated by including both the spin-spin[40] and spin-orbit contributions. The spin-spin zero-field splitting was obtained with the Γ-point approximation for the Brillouin zone sampling, while a denser k-point grid ($3\times3\times3$ Monkhorst-Pack set[41]) was imposed to achieve sufficient convergence of the spin-orbit zero-field splitting.

3 Results and Discussion

First, we used CW EPR spectroscopy to study the local environment of the paramagnetic Mn^{2+} ions in AmZn. The X- and Q-band CW EPR spectra of AmZn:Mn^{2+} powder recorded at different temperatures are presented in Figure 2 and S1 (see the Supplementary information), respectively. The obtained spectra show typical powder patterns of Mn^{2+} ions in $3d^5$ electron configuration ($^6S_{5/2}$ electronic ground state)[42–44]. The total electron spin of this state is $S = 5/2$, which provides five fine structure $\Delta m_S = \pm1$ transitions (m_S is the magnetic electron spin quantum number). For non-zero zero-field splitting, these transitions have different resonance fields, resulting in central ($m_S = -1/2 \leftrightarrow 1/2$) and outer ($\pm3/2 \leftrightarrow \pm1/2$ and $\pm5/2 \leftrightarrow \pm3/2$) fine structure lines. Each such line is further split into six due to the hyperfine interaction between the unpaired electrons and the ^{55}Mn nucleus[42–44]. The powder spectrum is more complicated compared to the single-crystal case, since the outer transitions occur at the extrema of the angular dependence of the fine structure. The central lines exhibit significantly less pronounced angular dependence resulting in a much higher intensity.

The X- and Q-band spectra of AmZn:Mn^{2+} consist of well-resolved central (Figures 2a, S1a) and outer (Figures 2b, S1b) fine structure lines. Upon cooling, the spectrum exhibits a pronounced change at about 190 K, which agrees with the phase transition temperature of this compound[23] indicating that the Mn^{2+} ions are sensitive to the transition. The existence of the outer fine structure lines and forbidden hyperfine transitions suggests a non-zero value of the zero-field splitting in both structural phases of the compound. Interestingly, upon cooling in the HT phase the outer transitions are slightly moving closer to the central lines implying a small decrease of the zero-field splitting. However, this behavior reverses in the LT phase, where a clear and strong increase of the zero-field splitting is observed on cooling. Note that in our previous EPR studies of the related Mn^{2+} doped $[(CH)_3NH_2][Zn(HCOO)_3]$ and $[(CH_3)_2NH_2][Cd(N_3)_3]$ frameworks[18,45], we observed a very sudden change of the fine structure due to the strong first-order phase transitions in these compounds.

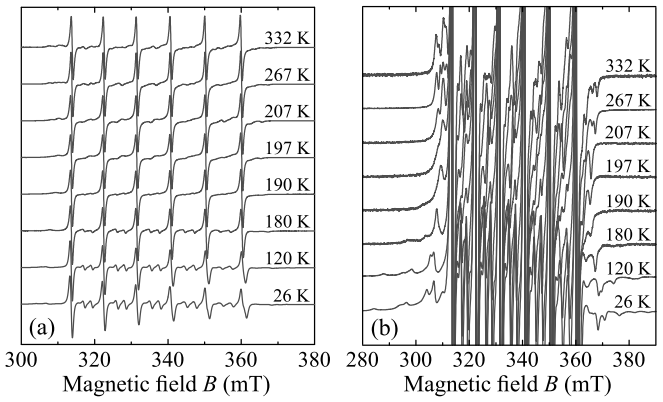

Fig. 2 (a) Central and (b) outer fine structure transitions of the temperature dependent X-band CW EPR spectra of AmZn:Mn^{2+}. The phase transition occurs at about 190 K.

To simulate the experimental spectra of AmZn:Mn^{2+}, we used the following spin Hamiltonian[44]:

$$H = \beta_e \boldsymbol{B}\boldsymbol{g}\boldsymbol{S} + \boldsymbol{S}\boldsymbol{A}\boldsymbol{I} + H_{FS}, \quad (1)$$

where the first term describes the electron Zeeman interaction characterized by the g-tensor $\boldsymbol{g}$ of the Mn^{2+} ion in the external magnetic field $\boldsymbol{B}$, and β_e denotes the Bohr magneton. The second term takes into account the hyperfine interaction described by the hyperfine coupling tensor $\boldsymbol{A}$. The last term of Eq. 1 describes the zero-field splitting, which can be expressed in terms of the extended Stevens operators $\boldsymbol{O}_k^q(\boldsymbol{S})$ as[46]

$$H_{FS} = \sum_k \sum_q B_k^q \boldsymbol{O}_k^q(\boldsymbol{S}). \quad (2)$$

Here $k = 2, 4, 6$, and $q = +k, ..., -k$. B_k^q are real coefficients that represent the magnitude of the corresponding zero-field splitting. The second-order axial D and orthorhombic E parameters can be expressed using these coefficients as $D = 3B_2^0$ and $E = B_2^2$. Usually, the higher-order zero-field splitting parameters are necessary to describe the high-spin Mn^{2+} and Fe^{3+} EPR spectra[44]. The fourth-order cubic a and axial F parameters can be expressed as $a = 24B_4^4$ and $F = 180B_4^0 - 36B_4^4$[44,46]. All expressions of the extended Stevens operators are given in Ref.[46]. In our simulations, the frames of a and F parameters are chosen to coincide with the fourfold axis of the cubic system[44]. It is also sufficient to use the isotropic $\boldsymbol{g}$ and $\boldsymbol{A}$ tensors (g and A_{iso} parameters, respectively) to obtain a good agreement with the experiment[42].

The simulation of the experimental X- and Q-band CW EPR spectra obtained at 100 K (LT phase) is presented in Figure 3 demonstrating a perfect agreement with the experiment. The simulations at both microwave frequencies were obtained using the same set of the spin Hamiltonian parameters: $g = 2.0013(2)$, $A_{iso} = -262(1)$, $D = -170(1)$, $E = 28(1)$, $a = 32(1)$, $F = -30(1)$, $B_4^{-1} = 2(2)$ and $B_4^{-2} = 0.5(2)$ MHz. Other fourth-order zero-field splitting parameters were set to zero.

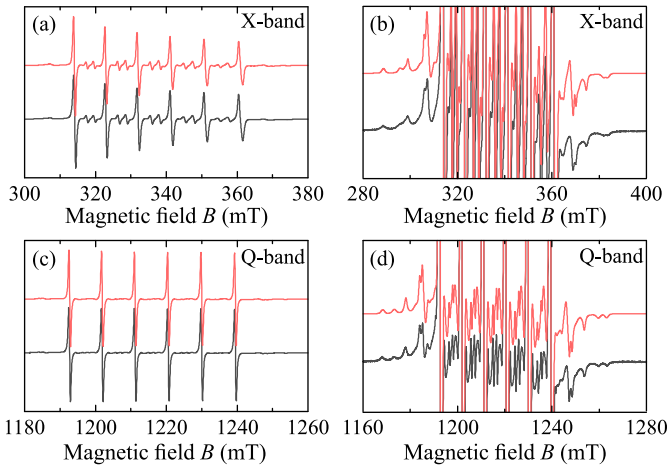

Fig. 3 Simulation of the X- and Q-band CW EPR spectra of AmZn:Mn^{2+} recorded at 100 K. Experimental and simulated spectra are shown in black and red, respectively. The emphasis is on the (a, c) central and (b, d) outer transitions.

The determined value of the isotropic hyperfine coupling constant A_{iso} is typical for the Mn-O coordination (see Ref.[42]) indicating that the Mn^{2+} ions successfully replaced Zn^{2+} and formed MnO_6 octahedra. Non-zero values of the axial D and E parameters show that these units are distorted, which is in agreement with the X-ray diffraction (XRD) measurements of both AmZn and AmMn compounds[11,23]. The Gaussian distribution of the axial and orthorhombic zero-field splitting parameters with the full width at half maximum of $\Delta D = 10(1)$ and $\Delta E = 7(1)$ MHz were used in the simulations to account for a slight line broadening (see Figure 3).

To support spectral simulations in the LT phase, we performed DFT calculations of the spin Hamiltonian parameters of Mn^{2+} centers in AmZn framework. Details of the Mn^{2+} coordination environment in the DFT-optimized supercell of AmZn are presented in Figure 4. The distances to the oxygen ligands indicate a distorted octahedral geometry far from the ideal D_{4h} symmetry. The calculated zero-field splitting tensor exhibits a large rhombic distortion with $E/D = 0.23$ (see Table 1). Although the rhombicity appears to be overestimated in comparison with the EPR results (e.g. $E/D = 0.13$ at 26 K, see also Figure S2), the calculated absolute value of D of 200.7 MHz is in a very good agreement with the experiment (see Table 1). Note that the sign of D has limited relevance close to the rhombic limit ($E/D = 1/3$, i.e. $D_{zz} \approx -D_{xx}$), where the principal axes can be altered by minor effects. The principal values of the spin-spin and spin-orbit contributions to the total zero-field splitting tensor $\boldsymbol{D} = \boldsymbol{D^{SS}} + \boldsymbol{D^{SO}}$ are $\boldsymbol{D^{SS}} = [-103.6; 17.1; 86.5]$ and $\boldsymbol{D^{SO}} = [-214.9; 6.1; 208.8]$ MHz.

Table 1 Measured and calculated absolute values of the zero-field splitting parameters (in MHz) of Mn^{2+} in AmZn.

Experiment				Theory		
T (K)	D	E	D/E	D	E	D/E
100	170	28	0.16	214.7	48.9	0.23
26	193	25	0.13			

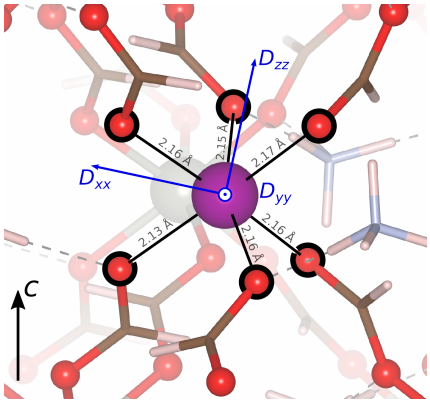

Fig. 4 The Mn^{2+} coordination environment in the DFT-optimized supercell of AmZn and the principal directions of the calculated zero-field splitting tensor.

The temperature evolution of the AmZn:Mn^{2+} EPR spectrum (Figure 2) indicates that D parameter should be much smaller close to the phase transition temperature as well as in the HT phase. This is confirmed by the simulations of the X- and Q-band spectra obtained at 199 K (slightly above T_0) (see Figure S3), which are in a good agreement with the experimental data. The determined fine structure parameters at this temperature are: $D = -20(5)$, $E = 2(1)$, $a = 45(1)$, $F = -40(1)$, $B_2^1 = 5(2)$, $B_2^{-1} = 2(1)$ and $B_2^{-2} = 19(2)$ MHz. Unfortunately, we were unable to precisely simulate the spectra at room temperature, but extensive trials of simulations indicate that D and E parameters should be very small or negligible at this temperature, and that the fine structure pattern is mainly determined by a, F and presumably some other higher-order fine structure parameters. Note that these parameters should be slightly higher at this temperature compared to 199 K case to account for a slightly wider spectrum at room temperature.

We further used pulse EPR and ENDOR experiments to confirm a successful incorporation of the Mn^{2+} ions in AmZn. The X- and Q-band echo-detected field sweep EPR spectra of AmZn:Mn^{2+} obtained at 15 K temperature and their corresponding simulations are presented in Figure 5. The best simulations were obtained using the following spin Hamiltonian parameters: $g = 2.0013(2)$, $A = -262(1)$, $D = -200(1)$, $E = 25(1)$, $a = 32(1)$, $F = -30(1)$, $B_4^{-1} = 2.5(1)$ and $B_4^{-2} = 1.8(5)$ MHz. The obtained parameters and linewidth are in a good agreement with the CW EPR results obtained at 26 K (see Figure S2). This confirms a uniform distribution of the Mn^{2+} centers in the crystal lattice of AmZn, as regions with a high local ion concentration would only contribute

to the CW spectra.

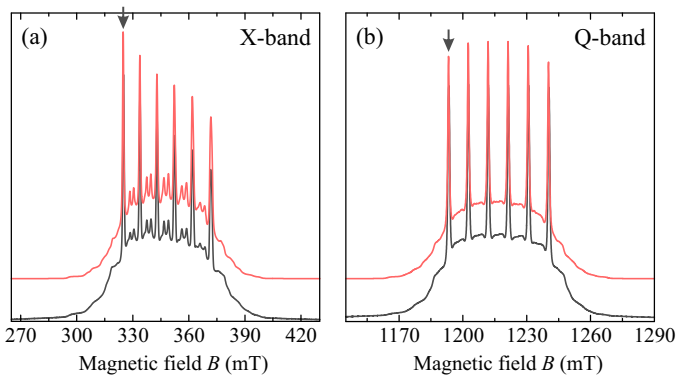

Fig. 5 Experimental (black) and simulated (red) (a) X- and (b) Q-band 2p echo-detected field sweep spectra of AmZn:Mn^{2+} recorded at 15 K. The arrows indicate field positions at which pulse EPR experiments were performed.

The proton hyperfine couplings with the Mn^{2+} ions in AmZn were determined using the Davies ENDOR spectroscopy. The obtained X- and Q-band ENDOR spectra measured at 15 K are presented in Figure 6 revealing three well-resolved ^{1}H hyperfine splittings of 2.6, 2.0 and 0.57 MHz at the perpendicular edge singularities of the powder pattern. Using the point-dipole approximation[31] and assuming a negligible isotropic component of the hyperfine couplings, these splittings translate into a ^{1}H-Mn^{2+} distance of 3.1, 3.4 and 5.2 Å, respectively. The analysis of the available structural data of AmZn reveals six formate protons that are within the $2.96-3.03$ Å distance from the metal center, while three nearest protons of NH_4^+ fall within $3.46-3.55$ Å distance range[23]. There are no protons in between these two distance sets. Thus, we assign the observed 2.6 and 2.0 MHz splittings to the formate and ammonium protons, respectively. The weakest hyperfine splitting of 0.57 MHz is more difficult to assign as protons from both ions could contribute to this signal. To verify the proton assignment, we performed spectral simulations using dipolar hyperfine couplings of 2.6, 2.0 and 0.57 MHz with the corresponding spectral weights of 2:1:0.7 (see Figure 6), where the 2:1 intensity ratio for 2.6 and 2.0 MHz lines is expected from the structural data. The simulated patterns are in a perfect agreement with the experiment verifying the structural model of AmZn and successful incorporation of the Mn^{2+} ions in this compound. Note that a similar hyperfine coupling of formate protons was also observed for the related Mn^{2+} doped $[(CH_3)_2NH_2][Zn(HCOO)_3]$ and $[CH_3NH_2NH_2][Zn(HCOO)_3]$ formates[28,47]. This indicates that ^{1}H hyperfine coupling of about 2.6 MHz could be used as a fingerprint for a successful Mn^{2+} ion incorporation into various formate frameworks.

We used ESEEM spectroscopy to further study the Mn^{2+} ion environment in AmZn. The X- and Q-band 3p ESEEM spectra of AmZn:Mn^{2+} recorded at 15 K are presented in Figure S4. The X-band spectrum obtained using the interpulse delay $\tau = 112$ ns shows a strong signal at 13.8 MHz, which corresponds to the Larmor frequency of protons. This signal also exhibits two shoulders indicating a poorly resolved substructure of the spectral line. The

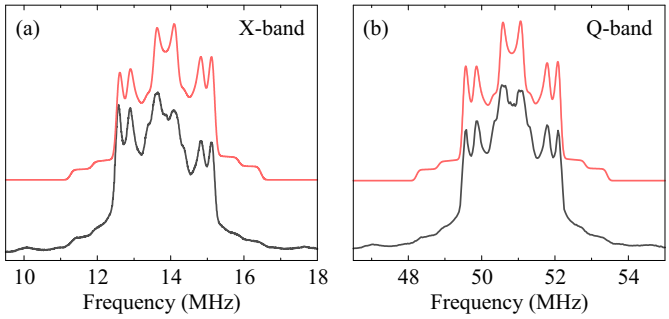

Fig. 6 (a) X- and (b) Q-band Davies ENDOR spectra of AmZn:Mn^{2+} recorded at 325.6 and 1193.3 mT, respectively. Measurements performed at 15 K. The simulated spectra are presented in red.

shoulders are separated by 2.6 MHz corresponding to the hyperfine coupling of formate protons as determined by the ENDOR experiment (Figure 6). The proton-suppressed ESEEM spectrum obtained using $\tau = 144$ ns[30] shows a very weak line at about 1.2 MHz, which may correspond to ^{14}N nucleus of the ammonium cation (see Figure S4a). This observation is supported by the Q-band 3p ESEEM spectrum depicted in Figure S4b, which reveals a weak signal at about 4 MHz. The structural data of AmZn indicates a relatively long N-Zn^{2+} distance of about 6.2 Å, which is likely the main reason for the weak ^{14}N ESEEM signal.

After proving a successful incorporation of the Mn^{2+} centers in AmZn, we go back to the analysis of the CW EPR results. By simulating the experimental CW EPR spectra obtained at different temperature, we determined the temperature dependence of the spin Hamiltonian parameters. The most significant change with temperature is observed for the axial zero-field splitting parameter D. The temperature dependence of the absolute value of this parameter is presented in Figure 7a revealing a gradual increase of $|D|$ below T_0. Such a behavior indicates a second-order or very weak first-order phase transition[48]. Note that the observed increase is much more continuous than observed for the related $[(CH)_3NH_2][Zn(HCOO)_3]$ and $[(CH_3)_2NH_2][Cd(N_3)_3]$ frameworks[18,45], which exhibit strong first-order (discontinuous) phase transitions.

We separated the phase transition contribution to D by subtracting a linear baseline (see Figure 7a), which may originate from a lattice contraction upon cooling or other effects independent on the transition. The obtained temperature dependence of the baseline-corrected D parameter is presented in Figure 7b revealing a typical behavior of an order parameter η[48].

Following this observation, the axial zero-field splitting parameter can be expanded in a series of η[49]:

$$D = \sum_m D_m \eta^m \qquad (3)$$

where D_m are the expansion coefficients. We can assume that the term D_1 vanishes, as we did not observe a splitting of the fine structure into two branches, which correspond to positive and negative values of η. Note that due to a presence of other zero-field splitting parameters, the positive and negative values of D provide different spectrum. By truncating higher order terms, the

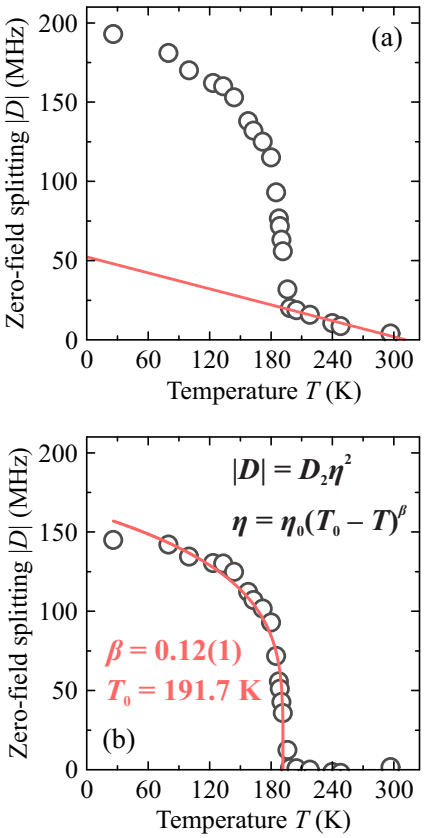

Fig. 7 (a) Temperature dependence of the axial zero-field splitting parameter D of the Mn^{2+} centers in AmZn. The solid line indicates the baseline fit. (b) Temperature dependence of D after baseline correction. The solid curve in (b) is the best power law fit. The error bars are smaller than data points.

zero-field splitting parameter can be approximated as

$$D \approx D_0 + D_2\eta^2, \tag{4}$$

where $D_0 = 0$ for the baseline-corrected data. For a second-order phase transition, the temperature dependence of η follows the power law[48]

$$\eta = \eta_0(T_0 - T)^\beta, \tag{5}$$

where η_0 is a constant, and β denotes a critical exponent of the order parameter.

The best fit of Eq. 4 to the experimental data is also presented in Figure 7b revealing a perfect agreement with the experiment. The determined phase transition parameters are: $T_0 = 191.7(5)$ K and $\beta = 0.12(1)$. The uncertainty of the fit parameters was determined by subtracting slightly different linear baselines from the temperature dependence of D (not shown).

The obtained value of the critical exponent β indicates a non mean-field behavior[50]. In addition, it falls within the universality class of either two-dimensional Ising ($\beta = 1/8$)[51] or two-dimensional three-state Potts ($\beta = 1/9$)[52] models. Note that a two-dimensional Ising behavior was also speculated for the phase transition in the related $[(CH_3)_2NH_2][M(HCOO)_3]$ frameworks[53], although a clear first-order character of the transition in these compounds[54] makes this observation highly controversial. Later it was demonstrated that the phase transition in these compounds can be described using a three-dimensional three-state Potts model[55], which, in agreement with the experimental data[54], exhibits a first-order phase transition[52].

Our result suggests a quasi two-dimensional ordering in AmZn, as β is usually much higher for phase transition models in three dimensions[56]. This is in agreement with the reported symmetry changes of this material at T_0[57]. During the transition, the twofold axis and twofold screw axis along the ab plane disappear, while the sixfold axis, threefold axis, and twofold screw axis along the c direction remain unchanged suggesting a quasi two-dimensional nature of the transition.

We further used pulse EPR to measure the temperature dependences of the longitudinal relaxation rate T_1^{-1} and the phase memory time T_m of Mn^{2+} centers in AmZn (see Figure 8). The measurements were performed only in the LT phase, as too fast spin decoherence prevented us to reach the phase transition temperature. The experimental points of T_1^{-1} were approximated using the following equation, which is frequently used to describe T_1 relaxation in ferroelectrics and related materials:[58]

$$T_1^{-1} = AT + B\mathrm{csch}^2(h\nu_{opt}/2k_BT). \tag{6}$$

Here the first term describes a direct (one-phonon) relaxation process with the acoustic lattice phonons. The second term takes into account a Raman (two-phonon) process of the optical phonon branch, which governs the longitudinal relaxation at higher temperature. ν_{opt} denotes the mode frequency, k_B is the Boltzmann constant, and A and B are the fit parameters. The best fit (Figure 8a) provides $\nu_{opt} = 4.16(4) \times 10^{12}$ Hz, which corresponds to $139(2)$ cm^{-1}. Note that IR and Raman studies of AmZn report phonon modes of similar frequency that involve motion of the metal-oxygen octahedra[13,26]. Our analysis indicates that the same vibrations are responsible for the longitudinal relaxation of the Mn^{2+} ions in AmZn at higher temperature.

Figure 8b shows the temperature dependence of the transverse relaxation of AmZn:Mn^{2+} in the ferroelectric phase revealing a monotonous decrease of the phase memory time T_m with increasing temperature. The value of T_m changes rather rapidly from about 550 ns at 25 K to 105 ns at 92 K, while at higher temperature the decrease is much more gradual. Unfortunately, we did not manage to probe the behavior of T_m at the phase transition point due to too fast relaxation. The observed temperature behavior of T_m likely indicates some dynamical process in the low-temperature phase of AmZn, which contributes to the transverse relaxation. At about 90 K, this process seems to slow down or change character causing much faster increase of T_m below this temperature. Note that a similar kink in the temperature behavior of T_m was also observed in the related Mn^{2+} doped $[(CH)_3NH_2][Zn(HCOO)_3]$ perovskite framework[28], where it is likely caused by the slowing down of the stochastic methyl group reorientation, which is followed by the tunneling dynamics[59]. The absence of methyl groups in AmZn requires a different relaxation mechanism. Indeed, XRD data of AmMg indicates that some ammonium cations still exhibit translational dynamics in the LT

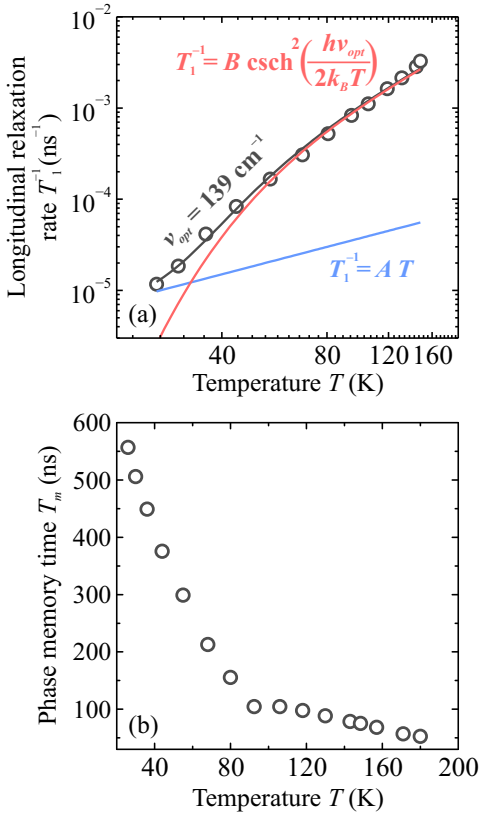

Fig. 8 Temperature dependence of the (a) longitudinal relaxation rate T_1^{-1} and (b) phase memory time T_m of the Mn^{2+} centers in AmZn. The curves in (a) are the total (black) and separate (blue and red) contributions to the longitudinal relaxation. Measurements performed at X-band microwave frequency (325 mT). The error bars are smaller than data points.

phase down to 120 K[15]. A similar behavior might be expected in AmZn, which could cause the kink in the T_m relaxation. On the other hand, we cannot fully disregard the onset of the tunneling dynamics of the ammonium cations at 90 K, which is frequently observed in various crystals[60]. However, we did not observe any unusual ESEEM modulations due to tunneling as was detected in $[(CH)_3NH_2][Zn(HCOO)_3]$[59].

4 Summary and Conclusions

In this work we reported a CW, pulse EPR and pulse ENDOR study of AmZn ferroelectric, which exhibits a structural phase transition at about 190 K. For these experiments, it was necessary to introduce a small amount of paramagnetic Mn^{2+} ion probes into the diamagnetic lattice of AmZn. This allowed us to monitor the changes in the local ion environment that are susceptible to the phase transition and dynamic effects.

The CW X- and Q-band EPR measurements of AmZn:Mn^{2+} revealed a successful incorporation of these ions into the structure at the zinc sites and formation of the MnO_6 octahedra. The temperature dependent spectra show a well resolved fine structure, which exhibits pronounced changes in the vicinity of the phase transition point. The spin Hamiltonian parameters of Mn^{2+} ions were obtained by simultaneously simulating the CW X- and Q-band spectra at different temperature. Simulations revealed a gradual increase of the axial zero-field splitting parameter during the transition resembling the behavior of the order parameter for a second-order (continuous) phase transition. The determined critical exponent of the order parameter is $\beta = 0.12(1)$, which belongs to either two-dimensional Ising or two-dimensional three-state Potts universality class. This suggests a quasi two-dimensional ordering in AmZn, which is in agreement with the reported symmetry changes during the transition.

Pulse EPR and ENDOR techniques were used to study the local environment and relaxation of the Mn^{2+} centers in AmZn. The X- and Q-band echo-detected field sweep EPR spectra were found to be in agreement with the CW results indicating a homogeneous distribution of the Mn^{2+} centers. The ENDOR spectroscopy was used to determine the proton hyperfine couplings with the manganese probe ions. The obtained X- and Q-band ENDOR spectra revealed at least three ^1H species close to the Mn^{2+} centers that are poorly resolved in the ESEEM experiments due to the weak hyperfine couplings. The obtained proton couplings were used to calculated the Mn–H distances, which are in a perfect agreement with the XRD data. This result confirmed incorporation of the Mn^{2+} ions and verified the previously reported structural model of AmZn.

Pulse EPR measurements of the longitudinal relaxation of the Mn^{2+} ions revealed that relaxation below 20 K is governed by a direct process with the acoustic lattice phonons. At higher temperature, an optical lattice mode dominates the relaxation via the two-phonon Raman process. The determined mode frequency of $139(2)$ cm^{-1} is in agreement with the previously reported Raman and IR results that show vibrations of the metal–oxygen octahedra in this frequency band. Unfortunately, too fast spin decoherence prevented us from measuring the T_1 relaxation at the phase transition point, where an anomalous increase of the longitudinal relaxation time can be expected for a ferroelectric compound[61]. The temperature dependence of the transverse relaxation time changes behavior at about 90 K, which may indicate onset of some dynamical process related to the ammonium ions of the compound.

Acknowledgements

This project has been funded by the Research Council of Lithuania (LMTLT) (agreement No. S-MIP-19-4). Numerical calculations were performed using grants of computer time from the Paderborn Center for Parallel Computing (PC2) and the HLRS Stuttgart. The Deutsche Forschungsgemeinschaft (DFG) is acknowledged for financial support (project No. 231447078-TRR 142).

References

1 B. Li, H.-M. Wen, W. Zhou and B. Chen, *J. Phys. Chem. Lett.*, 2014, **5**, 3468–3479.

2 J. Gandara-Loe, I. Ortuño-Lizarán, L. Fernández-Sanchez, J. L. Alió, N. Cuenca, A. Vega-Estrada and J. Silvestre-Albero, *ACS Appl. Mater. Interfaces*, 2019, **11**, 1924–1931.

3 P. Jain, V. Ramachandran, R. J. Clark, H. D. Zhou, B. H. Toby, N. S. Dalal, H. W. Kroto and A. K. Cheetham, *J. Am. Chem. Soc.*, 2009, **131**, 13625–13627.

4 Y. Tian, A. Stroppa, Y. Chai, L. Yan, S. Wang, P. Barone, S. Picozzi and Y. Sun, *Sci. Rep.*, 2015, **4**, 6062.

5 P. Jain, A. Stroppa, D. Nabok, A. Marino, A. Rubano, D. Paparo, M. Matsubara, H. Nakotte, M. Fiebig, S. Picozzi *et al.*, *npj Quantum Mater.*, 2016, **1**, 16012.

6 A. K. Cheetham and C. N. R. Rao, *Science*, 2007, **318**, 58–59.

7 M. Mączka, A. Gagor, B. Macalik, A. Pikul, M. Ptak and J. Hanuza, *Inorg. Chem.*, 2014, **53**, 457–467.

8 D. Di Sante, A. Stroppa, P. Jain and S. Picozzi, *J. Am. Chem. Soc.*, 2013, **135**, 18126–18130.

9 P. Jain, N. S. Dalal, B. H. Toby, H. W. Kroto and A. K. Cheetham, *J. Am. Chem. Soc.*, 2008, **130**, 10450–10451.

10 K. Asadi and M. A. van der Veen, *Eur. J. Inorg. Chem.*, 2016, **2016**, 4332–4344.

11 G.-C. Xu, W. Zhang, X.-M. Ma, Y.-H. Chen, L. Zhang, H.-L. Cai, Z.-M. Wang, R.-G. Xiong and S. Gao, *J. Am. Chem. Soc.*, 2011, **133**, 14948–14951.

12 M. Mączka, M. Ptak and S. Kojima, *Appl. Phys. Lett.*, 2014, **104**, 222903.

13 M. Mączka, K. Szymborska-Małek, A. Ciupa and J. Hanuza, *Vib. Spectrosc.*, 2015, **77**, 17–24.

14 R. Shang, S. Chen, K.-L. Hu, B.-W. Wang, Z.-M. Wang and S. Gao, *Chem.: Eur. J.*, 2016, **22**, 6199–6203.

15 M. Maczka, A. Pietraszko, B. Macalik and K. Hermanowicz, *Inorg. Chem.*, 2014, **53**, 787–794.

16 M. Maczka, A. Gagor, M. Ptak, W. Paraguassu, T. A. da Silva, A. Sieradzki and A. Pikul, *Chem. Mater.*, 2017, **29**, 2264–2275.

17 N. Abhyankar, S. Bertaina and N. S. Dalal, *J. Phys. Chem. C*, 2015, **119**, 28143–28147.

18 M. Šimėnas, A. Ciupa, M. Mączka, A. Pöppl and J. Banys, *J. Phys. Chem. C*, 2015, **119**, 24522–24528.

19 S. Bertaina, N. Abhyankar, M. Orio and N. S. Dalal, *J. Phys. Chem. C*, 2018, **122**, 16431–16436.

20 T. Besara, P. Jain, N. S. Dalal, P. L. Kuhns, A. P. Reyes, H. W. Kroto and A. K. Cheetham, *Proc. Natl. Acad. Sci.*, 2011, **108**, 6828–6832.

21 T. Asaji, S. Yoshitake, Y. Ito and H. Fujimori, *J. Mol. Struct.*, 2014, **1076**, 719–723.

22 M. Šimėnas, S. Balčiūnas, A. Ciupa, L. Vilčiauskas, D. Jablonskas, M. Kinka, A. Sieradzki, V. Samulionis, M. Maczka and J. Banys, *J. Mater. Chem. C*, 2019, **7**, 6779–6785.

23 G.-C. Xu, X.-M. Ma, L. Zhang, Z.-M. Wang and S. Gao, *J. Am. Chem. Soc.*, 2010, **132**, 9588–9590.

24 Z. Wang, B. Zhang, K. Inoue, H. Fujiwara, T. Otsuka, H. Kobayashi and M. Kurmoo, *Inorg. Chem.*, 2007, **46**, 437–445.

25 L. Gómez-Aguirre, B. Pato-Doldán, A. Stroppa, S. Yáñez-Vilar, L. Bayarjargal, B. Winkler, S. Castro-García, J. Mira, M. Sánchez-Andújar and M. Señarís-Rodríguez, *Inorg. Chem.*, 2015, **54**, 2109–2116.

26 M. Mączka, P. Kadłubański, P. T. C. Freire, B. Macalik, W. Paraguassu, K. Hermanowicz and J. Hanuza, *Inorg. Chem.*, 2014, **53**, 9615–9624.

27 J. Xu, B. E. Lucier, R. Sinelnikov, V. V. Terskikh, V. N. Staroverov and Y. Huang, *Chem.: Eur. J.*, 2015, **21**, 14348–14361.

28 M. Šimėnas, L. Macalik, K. Aidas, V. Kalendra, D. Klose, G. Jeschke, M. Mączka, G. Völkel, J. Banys and A. Pöppl, *J. Phys. Chem. C*, 2017, **121**, 27225–27232.

29 N. Abhyankar, S. Bertaina, M. Orio and N. S. Dalal, *Ferroelectrics*, 2018, **534**, 11–18.

30 A. Schweiger, *Angew. Chem., Int. Ed. Engl.*, 1991, **30**, 265–292.

31 A. Schweiger and G. Jeschke, *Principles of pulse electron paramagnetic resonance*, Oxford University Press on Demand, 2001.

32 L. Rowan, E. Hahn and W. Mims, *Phys. Rev.*, 1965, **137**, A61.

33 E. Davies, *Phys. Lett. A*, 1974, **47**, 1–2.

34 S. Stoll and A. Schweiger, *J. Magn. Reson.*, 2006, **178**, 42–55.

35 P. Giannozzi, S. Baroni, N. Bonini, M. Calandra, R. Car, C. Cavazzoni, D. Ceresoli, G. L. Chiarotti, M. Cococcioni, I. Dabo *et al.*, *J. Phys. Condens. Matter*, 2009, **21**, 395502.

36 P. Giannozzi, O. Andreussi, T. Brumme, O. Bunau, M. B. Nardelli, M. Calandra, R. Car, C. Cavazzoni, D. Ceresoli, M. Cococcioni *et al.*, *J. Phys. Condens. Matter*, 2017, **29**, 465901.

37 J. P. Perdew, A. Ruzsinszky, G. I. Csonka, O. A. Vydrov, G. E. Scuseria, L. A. Constantin, X. Zhou and K. Burke, *Phys. Rev. Lett.*, 2008, **100**, 136406.

38 S. Grimme, J. Antony, S. Ehrlich and H. Krieg, *J. Chem. Phys.*, 2010, **132**, 154104.

39 M. Cococcioni and S. De Gironcoli, *Phys. Rev. B*, 2005, **71**, 035105.

40 T. Biktagirov, W. G. Schmidt and U. Gerstmann, *Phys. Rev. B*, 2018, **97**, 115135.

41 H. J. Monkhorst and J. D. Pack, *Phys. Rev. B*, 1976, **13**, 5188.

42 V. Jain and G. Lehmann, *Phys. Status Solidi B*, 1990, **159**, 495–544.

43 S. K. Misra, *Phys. B*, 1994, **203**, 193–200.

44 A. Abragam and B. Bleaney, *Electron paramagnetic resonance of transition ions*, OUP Oxford, 2012.

45 M. Trzebiatowska, M. Maczka, M. Ptak, L. Giriunas, S. Balciunas, M. Šimėnas, D. Klose and J. Banys, *J. Phys. Chem. C*, 2019, **123**, 11840–11849.

46 I. D. Ryabov, *Appl. Magn. Reson.*, 2009, **35**, 481.

47 M. Šimėnas, S. Balčiūnas, M. Trzebiatowska, M. Ptak, M. Mączka, G. Völkel, A. Pöppl and J. Banys, *J. Mater. Chem. C*, 2017, **5**, 4526–4536.

48 B. Strukov and A. Levanyuk, *Ferroelectric phenomena in crystals: Physical foundations*, Springer-Verlag, Berlin, 1998.

49 F. J. Owens, C. P. Poole and H. A. Farach, *Magnetic resonance of phase transitions*, Academic Press, 2013.

50 M. E. Lines and A. M. Glass, *Principles and applications of ferroelectrics and related materials*, Oxford university press, 2001.

51 C. N. Yang, *Phys. Rev.*, 1952, **85**, 808–816.

52 F. Y. Wu, *Rev. Mod. Phys.*, 1982, **54**, 235–268.

53 K. D. Hughey, A. J. Clune, M. O. Yokosuk, J. Li, N. Abhyankar, X. Ding, N. S. Dalal, H. Xiang, D. Smirnov, J. Singleton *et al.*, *Inorg. Chem.*, 2018, **57**, 11569–11577.

54 M. Sánchez-Andújar, L. Gómez-Aguirre, B. P. Doldán, S. Yáñez-Vilar, R. Artiaga, A. Llamas-Saiz, R. Manna, F. Schnelle, M. Lang, F. Ritter *et al.*, *CrystEngComm*, 2014, **16**, 3558–3566.

55 M. Šimėnas, S. Balčiūnas, M. Mączka, J. Banys and E. E. Tornau, *Phys. Chem. Chem. Phys.*, 2016, **18**, 18528–18535.

56 A. Pelissetto and E. Vicari, *Phys. Rep.*, 2002, **368**, 549–727.

57 T. Hang, W. Zhang, H.-Y. Ye and R.-G. Xiong, *Chem. Soc. Rev.*, 2011, **40**, 3577–3598.

58 H.-E. Müller, G. Völkel, W. Brunner, P. Cevc and I. Kurkin, *Phys. Status Solidi B*, 1987, **141**, 343–349.

59 M. Šimėnas, D. Klose, M. Ptak, K. Aidas, M. Mączka, J. Banys, A. Pöppl and G. Jeschke, *Sci. Adv.*, 2020.

60 N. Verdal, T. J. Udovic, J. J. Rush, V. Stavila, H. Wu, W. Zhou and T. Jenkins, *J. Chem. Phys.*, 2011, **135**, 094501.

61 G. Völkel, H.-E. Müller and W. Flohrer, *Phys. Status Solidi B*, 1981, **108**, 501–506.